

A Novel Manipulator for Percutaneous Needle Insertion: Design and Experimentation

Harmanpreet S. Bassan, Rajni V. Patel, *Fellow, IEEE*, and Mehrdad Moallem, *Member, IEEE*

Abstract—In this paper, we present the design of a novel 5-DOF manipulator for percutaneous needle insertion. The requirements of the manipulator have been instigated by a relatively common medical procedure: low-dose rate brachytherapy of the prostate. The manipulator can perform orientation, insertion, and rotation of the needle and linear motion of the stylet to drop radioactive seeds contained in a thin hollow needle (cannula) at targeted locations. The key features of the manipulator such as backdrivable joints, a fault-tolerant needle driver, stationary actuators, and redundant sensors enhance overall safety and reliability of the mechanism, a critical requirement for surgical manipulators. The manipulator is an integral part of a system utilizing a mechanically rotated side-firing transducer to create 3-D ultrasound images of the organ and utilizing 3-D SLICER software to visualize those images. Experimental results in agar phantoms prove that the manipulator is capable of positioning the needle tip at the targeted locations with good accuracy.

Index Terms—Image-guided surgery, manipulator design, percutaneous needle insertion, prostate brachytherapy.

I. INTRODUCTION

THE PROSTATE is a small exocrine gland in men responsible for the production of the liquid component of the seminal fluid. A normal prostate is about 40 cm^3 in volume and is surrounded by other organs such as the bladder, the urethra, the rectum, and the seminal vesicles. In the later stages of life, a common malignancy of the prostate is the growth of abnormal cells in the organ, termed as prostate cancer. An early-stage localized prostate cancer can have symptoms such as frequent urination, blood in urine, painful urination, difficulty achieving erection, and painful ejaculation. In its advanced stages, prostate cancer can metastasize to lymph nodes and through the blood stream to other parts of body, potentially becoming a life-threatening condition. It is reported [1] that prostate cancer accounted for 186,320 new cases and 28,660 deaths in the

United States in 2008. It is found at autopsy in 30% of men at the age of 50, 40% at age 60, and almost 90% at age 90, and is the second leading cause of cancer deaths in men after lung cancer [2].

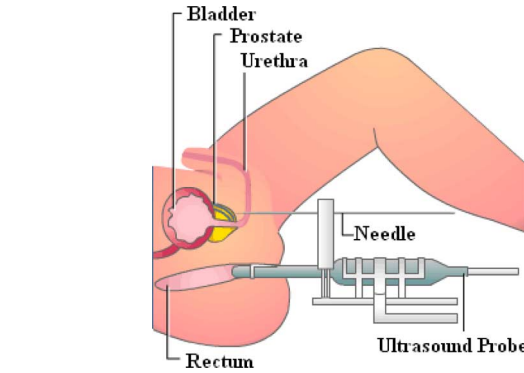


Fig. 1. TRUS-guided LDR brachytherapy.

United States in 2008. It is found at autopsy in 30% of men at the age of 50, 40% at age 60, and almost 90% at age 90, and is the second leading cause of cancer deaths in men after lung cancer [2].

Early-stage diagnosis and therapy of prostate cancer can be highly effective in decreasing the mortality associated with the disease. Even at later stages, the treatment for prostate cancer can be effective. Brachytherapy is a form of radiation therapy that involves insertion of radioactive isotopes into the gland either temporarily (known as high-dose rate (HDR) brachytherapy) or permanently (known as low-dose rate (LDR) brachytherapy) to affect therapy. The more recent approach to LDR brachytherapy is the transperineal technique in which slender needles carrying radioactive seeds are inserted into the prostate through the area between the scrotum and the anus [3]. The patient is put under general anesthesia in a lithotomy position and a stepper assembly that includes a transrectal ultrasound (TRUS) probe and a rectilinear template grid is brought into the neighborhood of the perineum. The probe is carefully inserted and adjusted into the patient's rectum until satisfactory images of the organ are obtained. The surgeon then inserts preloaded needles through equally spaced passages on the template grid based on a preplanned dosimetry. Once at the target location, the cannula is retracted while keeping the stylet stationary to drop the radioactive seeds. A typical procedure could involve somewhere between 15 and 20 needles with a total of 80–100 seeds. A postoperative radiograph or computed tomography (CT) scan is performed to assess the adequacy of the implantation and ensure that no seed has found its way into the neighboring bladder or the rectum. The radiation in the seeds decay over a period of time affecting therapy and eventually becoming inert. The treatment results in a highly conformal dosimetry while sparing surrounding organs from harmful exposure [4]. Fig. 1 shows a manual TRUS-guided prostate brachytherapy setup [5].

Manuscript received April 25, 2008; revised September 18, 2008. First published March 27, 2009; current version published November 11, 2009. Recommended by Technical Editor J. P. Desai. This work was supported by the Natural Sciences and Engineering Research Council (NSERC) of Canada under a Collaborative Health Research Project Grant (262583–2003) and by infrastructure grants from the Canada Foundation for Innovation awarded to UWO (R. V. Patel).

H. S. Bassan is with the Department of Electrical and Computer Engineering, The University of Western Ontario, and Canadian Surgical Technologies and Advanced Robotics (CSTAR), London, ON, Canada (e-mail: hbassan@uwo.ca).

R. V. Patel is with the Department of Electrical and Computer Engineering and the Department of Surgery, The University of Western Ontario, and Canadian Surgical Technologies & Advanced Robotics (CSTAR), London, ON, Canada (e-mail: rvpatel@uwo.ca).

M. Moallem is with the School of Engineering Science, Simon Fraser University, Surrey, BC V3T 0A3, Canada (e-mail: mmallem@sfu.ca).

Color versions of one or more of the figures in this paper are available online at <http://ieeexplore.ieee.org>.

Digital Object Identifier 10.1109/TMECH.2009.2011357

In this paper, we describe the design and evaluation of a novel robotic system for performing TRUS-guided LDR brachytherapy. The paper is organized as follows. Section II describes the limitations of the present manual approach to LDR brachytherapy. Section III reviews the previous work on developing robotic systems for percutaneous needle insertion. Section IV describes the kinematic structure of the manipulator. Section VI describes the design of 3-D ultrasound system. In Section VII, experimental results are presented for the joint tracking and needle targeting experiments in free air and agar phantoms. A brief discussion is presented in Section VIII, and Section IX contains concluding remarks.

II. LIMITATIONS OF PRESENT APPROACH

The accuracy of the TRUS-guided prostate brachytherapy procedure depends on how close the seeds are to their targeted locations and is highly dependent on the dexterity and experience of the surgeon. The inherent flexible nature of the needles also causes them to deflect during insertion, making needle insertion even more difficult. Multiple insertions are often required before the needle tip hits the target area, causing significant trauma [6] to the prostate and longer procedure times. The 2-D nature of ultrasound images makes it difficult to visualize needle trajectory during insertion, and the surgeon is often required to make a mental picture of the anatomy during the procedure. Further, the horizontal template grid restricts needle travel along parallel trajectories. This limitation prevents patients suffering from benign prostate hyperplasia (BPH, enlargement of the prostate) to undergo brachytherapy due to pubic arch interference [7]. Another disadvantage of the present approach is the delay between preplanning and the actual procedure. During this time, the location or size of the prostate can change significantly [8]; thus, optimal dosimetry cannot be ensured. At the same time, edema during the procedure [9] can also cause the organ to swell significantly resulting in misplaced seeds. In the present approach, no online dosimetry can be performed to compensate for such changes, and hence, inaccuracies in the therapy can result.

III. ROBOT-ASSISTED NEEDLE INSERTION

Robot-assisted percutaneous needle insertion has been proposed by several researchers in recent years. A robotic approach to needle insertion can overcome some of the shortcomings of the manual approach. A robotic device can insert needles with consistent accuracy and eliminate the need of a template grid altogether. Thus, it is possible to insert needles along oblique trajectories and patients deemed ineligible for brachytherapy due to pubic arch interference can be treated through the robotic insertion approach. Another advantage of a robotic system is that it can be integrated with an imaging modality to achieve an image-guided system. The system can also cut down on procedure times by merging dose planning and therapy in a single session. Another advantage of robotic needle insertion under “real-time” ultrasound guidance is the possibility of online dosimetry. Any changes in the organ size or errors in seed

placement can be compensated to a certain extent by intraoperatively updating the dosimetry to define new target points for the remaining needles. This feature would require modification to commercially available dosimetry software and is outside the scope of this paper.

Some mechatronic systems (including robots) for needle insertion have been reported in the literature. One such system utilizing TRUS and CT guidance for percutaneous needle insertion is reported in [10] and [11], respectively. The robot consists of three independent stages for needle positioning, orientation, and insertion. The mechanism, however, does not include support for needle rotation or stylet motion. Further, the friction-based needle transmission [12] employed in the manipulator has been shown to exhibit slippage resulting in needle placement errors. A manipulator capable of performing biopsies using TRUS is described in [13]; however, only 1 DOF is motorized at present. Using an industrial manipulator and a manual needle insertion guide, a system for ultrasound-guided biopsies has been reported in [14]. A mechanism for percutaneous needle insertion is described in [15]; however, the system lacks the capability to perform oblique needle insertion. Another mechanism is described in [16] for percutaneous needle insertion that utilizes two planar XY stages to achieve a remote center of motion (RCM) constraint. Needle insertion is performed manually and no provision is made for the stylet motion. A second generation of the device is reported in [17]. This design utilizes two 7-DOF passive arms mounted on a bridge to perform the gross positioning and a 2-DOF positioning module to perform needle orientation. A manipulator for ultrasound-guided needle insertion is presented in [18]. The manipulator consists of a 5-DOF passive arm to position the needle tip at the skin entry point and a 2-DOF active driver for needle insertion. Needle insertion is accomplished using a friction-based drive mechanism similar to [10], and no provision is provided for needle rotation or stylet motion. Manual needle insertion is compared in [19] with a robotic needle insertion *in vivo* in terms of positioning accuracy and applied forces. Transrectal access to the prostate is utilized in [20] to perform needle insertion. However, transrectal access can only be utilized for procedures involving a few needle insertions such as biopsies, and hence, this approach is somewhat limited for therapy. Another approach to percutaneous needle insertion based on a hand-held needle driver is described in [21]. The device lends itself well to single needle insertion tasks such as biopsy. In therapy, where multiple needle insertions are required, it is difficult to keep such a device stationary for long periods of time without any support. Thus, precise needle placement becomes difficult. Recently, a 16-DOF robotic system for ultrasound-guided prostate brachytherapy is presented in [22]. A 4-DOF needle guiding device for prostate brachytherapy is presented in [23]. The mechanism is capable of positioning the needle in a plane and orienting it about the yaw and pitch axes. Needle insertion, rotation, and seed placement are conducted manually, and preliminary needle insertion results in a prostate phantom are provided.

In addition to mechanisms utilizing ultrasound guidance, various systems are also reported for CT and magnetic resonance imaging (MRI)-guided percutaneous needle insertion. The

design constraints and requirements for such systems are quite different from systems employing ultrasound guidance. A 2-DOF manipulator for percutaneous needle insertion is described in [24] using CT as the imaging modality. Another manipulator employing a parallel structure for CT-guided percutaneous needle insertion is reported in [25] and [26]. The mechanism is designed to strap on the patient and is small enough to fit inside the bore of a CT scanner. The three-legged parallel structure positions and orients the needle along the desired trajectory, and a 2-DOF passive/active needle driver is utilized for needle insertion and rotation.

Utilizing MRI, a mechanism for needle insertion is described in [27]. The design utilizes planar drives similar to those of [16] to create an RCM. The size of the manipulator is quite large and is unsuitable for integration with an ultrasound system. A 7-DOF manipulator for MRI-guided interventions is presented in [28]. The mechanism includes an *XYZ* Cartesian positioner, 2 DOF for rotation for needle orientation, 1 DOF for rotation about needle axis, and a linear drive for needle translation. A robotic device for MRI-guided breast interventions is presented in [29]. The device includes a combination of manual- and computer-controlled motions for percutaneous needle insertion. A 2-DOF MRI-guided prostate biopsy robotic system is presented in [30]. The system employs optical position measurements and piezoceramic motors to minimize interference with magnetic fields of the MRI system. An MRI-compatible manipulator employing parallel kinematics and novel pneumatic stepper motor is described in [31]. The mechanism is capable of fully automated seed placement inside the patient's prostate. Another manipulator for percutaneous needle insertion using MRI guidance is presented in [32]. Needle placement results for a 2-DOF experimental prototype in a gel phantom are presented. An MRI-compatible manipulator employing piezoelectric actuators is described in [33]. Preliminary needle insertion results in a gel phantom are given.

A robot for treatment of prostate cancer using high-intensity focused ultrasound is described in [34]. However, this form of therapy has not gained much interest as yet and is still at an investigational stage.

The objective of this paper is the design of a manipulator for ultrasound-guided prostate brachytherapy. TRUS is particularly widespread in the diagnosis and therapy of the prostate cancer due to its easy availability and low cost. Furthermore, since this imaging modality does not utilize any radiation, it can be employed throughout the procedure without any adverse side effects to the patient or the clinicians. The novelty of the prototype robotic system presented here lies in the fact that all DOFs of the manipulator are actively controlled. Therefore, the task of needle insertion as well as seed placement can be executed under computer control. In addition, the backdrivable joints of the manipulator also lend themselves to manual control, if desired. The concept of a novel fault tolerant needle driver applied in the design has also not been reported elsewhere. The integration of a force sensor with the manipulator allows the possibility of implementation of various control strategies to minimize needle deflection based on force/position information, a feature lacking in various previous designs.

IV. MECHANISM DESIGN

In order to get an idea of the space constraints in the operating room, several actual brachytherapy procedures were observed. Simultaneously, discussions were held with clinicians on the required DOFs. Based on this information, a set of preliminary requirements for the manipulator was prepared.

- 1) The manipulator should be able to position the needle tip at any arbitrary point of entry.
- 2) It should be capable of performing needle insertion along oblique trajectories.
- 3) There should be a provision to rotate the needle about its longitudinal axis in order to implement approaches for reducing needle deflection and to perform corrective action.
- 4) The manipulator should be able to satisfy the space constraints [22] of a typical TRUS-guided prostate brachytherapy procedure.

The task of percutaneous needle insertion can be considered as a sequential task: bring the needle tip in contact with the point of entry, perform needle orientation along the desired trajectory, translate and rotate the needle about its longitudinal axis until the needle tip reaches the target, and lastly, keep the stylet stationary and retract needle sheath to drop radioactive seeds.

Therefore, it was decided that the kinematic structure of the robotic system should be based on a two-tier design, a macro-micro system. The macro-micro approach has been applied in the past to percutaneous procedures, e.g., in [11] and [18]. The macro stage is responsible for the gross motions and is used to position the needle tip at the skin entry point. Once positioned, the macro stage can then be locked in place to avoid any unwanted motions.

The micro-manipulator carries out finer motions and performs the orientation and insertion of the needle and is the focus of this paper. A particularly useful kinematic structure for the micro-manipulator is that having an RCM constraint. This constraint allows a surgical tool (i.e., needle, laparoscope, etc.) to be reoriented about a pivot point. This pivot point is located distal to any of the linkages or bearings of the manipulator along the axis of the surgical tool and is often termed the RCM point. Commonly, the manipulator is positioned such that the pivot point coincides with the skin entry point. These mechanisms are useful and safer for surgical applications due to the fact that the pivot point does not translate for any motion of the RCM joints, and hence cannot apply lateral forces on the skin. Remote center kinematics can be accomplished using controlled redundant RCM [35], passive RCM [36], or mechanically constrained RCM [37], [38].

A comparative analysis was performed between a spherical-linkage-based RCM design and a double-parallel-rectangle-based RCM design. A double-parallel-rectangle-based structure was found to be advantageous in terms of the number of required actuators, precision, simplicity of control, and simpler design. This design has been applied for surgical applications, e.g., in [39]–[41]. A key advantage of the double parallelogram structure is that it is possible to position the RCM actuators on the stationary part of the manipulator to minimize the mass of moving linkages. It is also possible to route transmission elements

for the distal joints over the parallelogram linkages as accomplished in [42]. A double-parallelogram-based structure can also be easily counterbalanced as compared to spherical linkages.

Once the kinematic structure of the robotic system was finalized, a set of formal requirements for the micro robotic system was created as follows.

- 1) The mechanism should be backdrivable, i.e., in case of an emergency, a clinician should be able to manually move the manipulator away.
- 2) Each of the primary DOFs (i.e., first four DOFs: two RCM, needle translation, and rotation) of the micro-manipulator should have emergency brakes to ensure safety.
- 3) Although the brakes prohibit any undesirable motions of the manipulator in case of power failure, extra safety should be added by gravity balancing the first two joints (double parallelogram structure) of the manipulator.
- 4) The actuators driving the primary DOFs should be stationary, i.e., they should not travel with the links of the manipulator. This adds extra safety to the system, because the links of the manipulator can be made lightweight.
- 5) Redundant sensors should be installed on the primary DOFs for safety.
- 6) The positioning accuracy of the manipulator should be better than 2 mm (clinically acceptable error).
- 7) A 6-DOF force sensor should be employed to measure needle–tissue interaction. This information will be used to reduce needle deflection and provide a clinician with feedback of the forces acting on the needle through the use of a haptic device.
- 8) The overall weight of the micro-manipulator should be less than 5 kg. This figure was obtained based on initial computer-aided design (CAD) designs and a review of off-the-shelf actuators with brake–encoder combinations. The macro stage was designed to carry such a load.

A modification was made to introduce a tool offset that allowed the stationary section of the manipulator to be moved away from the patient, leading to better clearance. At the same time, introduction of the tool offset required modification to the double parallelogram structure in order to maintain the RCM constraint. Fig. 2 shows the modified double parallelogram mechanism employed in the micro-manipulator.

The value of angle ϕ_3 for link 3 can be computed as

$$\phi_3 = \sin^{-1}(d_t/l_3) \quad (1)$$

where l_3 is the length of the front section of link 3 and d_t is the tool offset. In our case, $l_3 = 160$ mm and $d_t = 51.5$ mm, which gives $\phi_3 = 18.776^\circ$.

A. Cable-Based Transmission

The first and second joints of the manipulator employ a stainless steel cable (model SP2047, 7×49 construction, Sava Industries, NJ, USA) based transmission. One of the important characteristics of this cable is very low stretch that ensures good positioning accuracy. The resulting mechanism employing this transmission is backdrivable and exhibits very low friction. The transmission ratio in this case is given as the ratio of the mo-

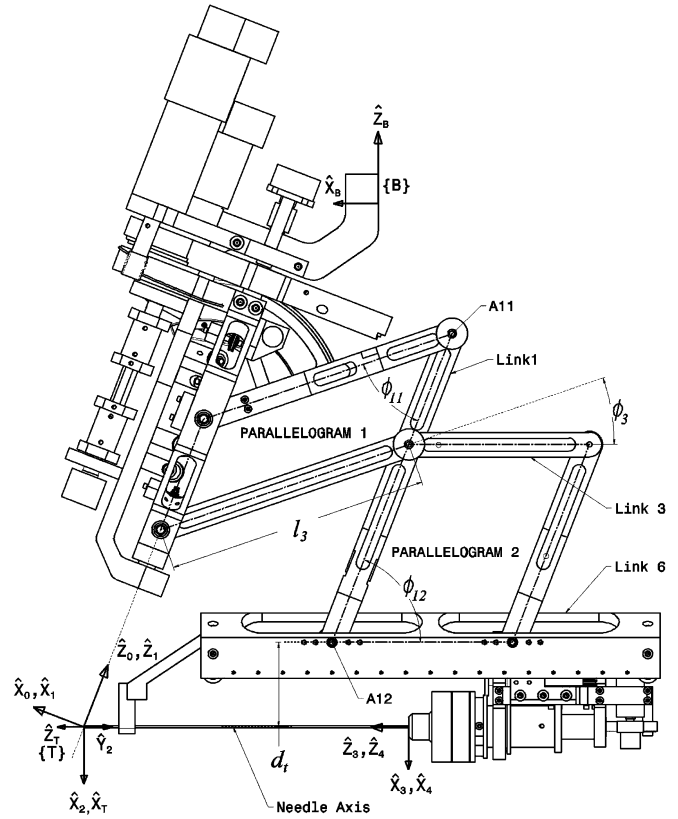


Fig. 2. Modified double parallelogram and D-H frame assignment.

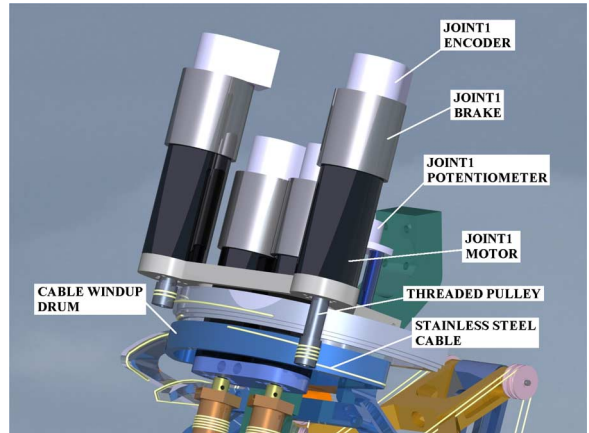


Fig. 3. CAD model of joint 1 cable transmission.

tor pulley diameter to the cable windup drum diameter. Fig. 3 shows the CAD model of the cable-based Transmission for the first joint of the micro-manipulator.

A conventional parallelogram mechanism requires one of the RCM actuators (second axis) to move with the linkages of the mechanism as in [42]. In order to reduce the mass of this actuator, either a high gear ratio is applied (as accomplished in [43]) or a large cable windup drum is employed (as in [42]). In the micro-manipulator, a cable-driven transmission based on [44] was implemented that allowed the second actuator to be located on the stationary part of the manipulator, thereby reducing the

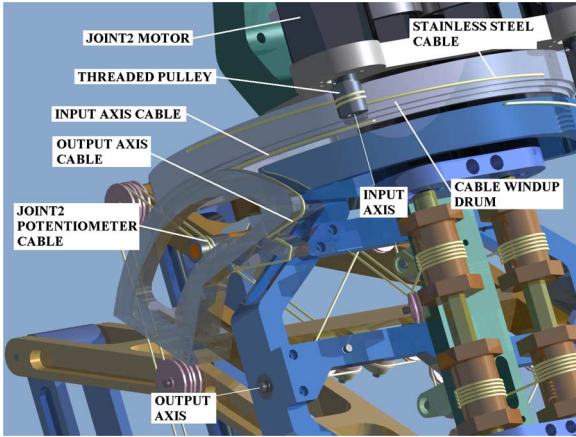


Fig. 4. CAD model of joint 2 cable transmission.

mass of the moving linkages. Fig. 4 shows the CAD model of the cable-based transmission for the second joint of the micro-manipulator.

As shown in Fig. 4, the transmission transfers the torque between two axes that are nonintersecting and orthogonal to each other. The input torque is supplied by the joint 2 motor to the cable windup drum through a cable transmission similar to joint 1. A second cable transmission transfers torque from the cable windup drum to the output axis (second joint) through the use of two stainless steel cables (input axis and output axis cable). A third cable-based transmission is utilized to measure the absolute value of the joint 2 angle through a multturn potentiometer. This topology allows for the placement of the joint 2 actuator on the stationary part of the manipulator. The first and second joints are actuated by Maxon dc brush type motors (Model RE35 with integrated brakes and HEDL5540 500 counts per revolution (CPR) encoders). As an added safety measure, each of these joints has redundant joint sensors (potentiometers). These are also utilized to bring the manipulator to its home position.

B. Novel Fault-Tolerant Needle Driver

The third and fourth joints of the micro-manipulator achieve linear motion of the needle along the desired trajectory and rotary motion about its longitudinal axis, respectively.

The micro-manipulator employs a novel cable-based differential drive transmission to achieve the translation and rotation of the needle. The drive is fault tolerant to a single actuator failure, and it is possible to perform needle insertion under computer control even if such a fault occurs. Thus, the mechanism exhibits enhanced safety as compared to the conventional approach. Furthermore, the translation error at the needle tip in the case of a differential drive is reduced to half, and half the error appears as error in rotation. This rotational error has minimal effect on seed placement accuracy. Thus, overall the differential drive provides higher positioning accuracy when compared to the conventional approach. Another benefit of the cable-based differential drive is that both actuators are stationary; hence, the mass of moving linkages is reduced. These actuators can be located proximally on the stationary part of the manipulator, further reducing the

mass of the moving parts. The cable-driven differential can be easily designed to be backdrivable so that the needle can be manually extracted, if required, without the need for a quick disconnect mechanism.

The output torque in case of a differential-cable-based transmission for the micro-manipulator is given by

$$\tau_t = \tau_{M3} + \tau_{M4} \quad (2)$$

and

$$\tau_r = \tau_{M3} - \tau_{M4} \quad (3)$$

where τ_t is the output torque (needle translation) and τ_r is the output torque (needle rotation), respectively. τ_{M3} and τ_{M4} are actuator 3 and actuator 4 input torques, respectively.

It is clear from (2) and (3) that both actuator 3 and actuator 4 work in unison to provide needle translation and rotation torque, respectively. The output translation torque τ_t is the summation of actuator 3 torque and actuator 4 torque, and the output rotation torque τ_r is the difference of actuator 3 torque and actuator 4 torque. It is evident that in case of a single actuator failure (for example, say actuator 3), the other actuator (actuator 4) in this mechanism is still capable of delivering output torque for needle translation as well as needle rotation. Thus, a single uninterrupted needle insertion can be performed in spite of a single actuator failure using this approach, and therefore, overall safety in the system is increased substantially. Another advantage of the differential mechanism is apparent from (2) and (3). In case of needle insertion, significantly higher torque is required in the direction of needle translation and relatively smaller torque is required for needle rotation. In the differential mechanism, both actuators apply additive torque in the direction of needle translation and subtractive torque in the direction of needle rotation. Thus, roughly, each actuator should be capable of exerting about half of the maximum required torque in the needle translation.

The value of the maximum static torque (under no fault condition) that each of the actuators 3 and 4 should be capable of exerting is given as

$$\tau_{M3\max} = \tau_{M4\max} \approx \frac{\tau_{t\max} + \tau_{r\max}}{2}. \quad (4)$$

From (4), it is clear that in the case of a differential drive, both actuators could be selected with similar torque ratings and similar size. This reduces the cost associated with the actuators and respective drive electronics. For the micro-manipulator, joints 3 and 4 are actuated by Maxon dc brush-type motors (Model RE35 with integrated brakes and HEDL5540 500 CPR encoders) and have redundant potentiometers (Model 3540S-1-502L from Bourns, Inc., USA) to enhance safety.

Through the use of a remote tendon actuation scheme, actuators 3 and 4 can be located proximally on the rigid section of the manipulator. As shown in Fig. 5, these tendons transfer actuator torque to the needle translation and rotation assembly over idler pulleys on the intermediate links. A key obstacle in designing a remote tendon actuation scheme is that the tendons have to maintain a constant length irrespective of any motions of the intermediate linkages in order to eliminate slack. As shown in Fig. 5, there are four pivot axes that are affected by motions

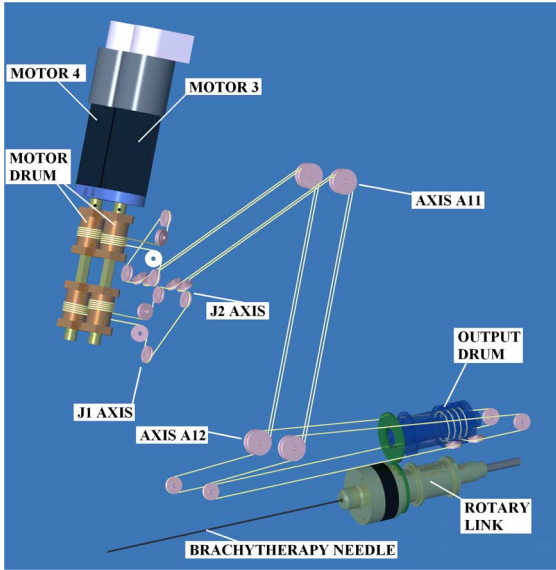


Fig. 5. Cable routing for needle translation and rotation.

of intermediate links; J1, J2, A11, and A12. Axes J1 and J2 are the first and second joint axes, respectively, and intersect each other. In order to maintain constant tendon length at these axes, tendons are routed over idler pulleys such that tendon changes plane along these joint axes. Thus, any joint motion causes a simple twisting motion of the tendon, and hence does not change tendon length.

For link 1, angles ϕ_{11} and ϕ_{12} about axes A11 and A12 are, respectively (see Fig. 2), related as

$$\phi_{11} = 118.56^\circ - \phi_{12}. \quad (5)$$

The double parallelogram linkages impose a constraint that any increase in the value of the angle ϕ_{11} is accompanied by equal decrease in the value of the angle ϕ_{12} and vice versa. Thus, the overall change in tendon length as a result of motion about these axes is canceled out. A low-stretch multibraided tungsten cable (8 × 19 construction, Strand Products, CA, USA) with a breaking strength of 49 pounds was chosen for the tendons for the manipulator.

C. Needle Assembly

The needle translation and rotation assembly consists of three main components: DistalFrame, OutputDrum, and RotaryLink. Fig. 6 shows the needle assembly for the micro-manipulator.

The DistalFrame can freely translate with respect to the DistalSupport (Fig. 7) through the use of miniature circulating ball carriages that create a low-friction prismatic joint. Each side of the DistalFrame is attached to a carriage that slides over the corresponding guide rail on the DistalSupport to achieve the linear motion. Fig. 7 shows the prismatic joint for needle translation.

Two low-friction rotary joints (OutputDrum and DistalFrame) and (RotaryLink and DistalFrame) are created through the use of four-point contact ball bearings. The OutputDrum is also geared to the RotaryLink through the use of a 1:1 spur gears. Overall, this assembly serves four purposes: provides tendon

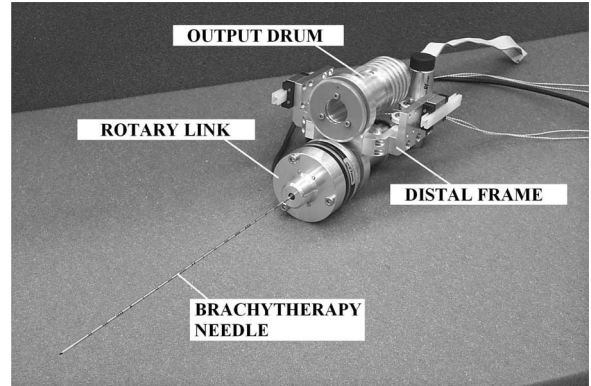


Fig. 6. Distal stage assembly.

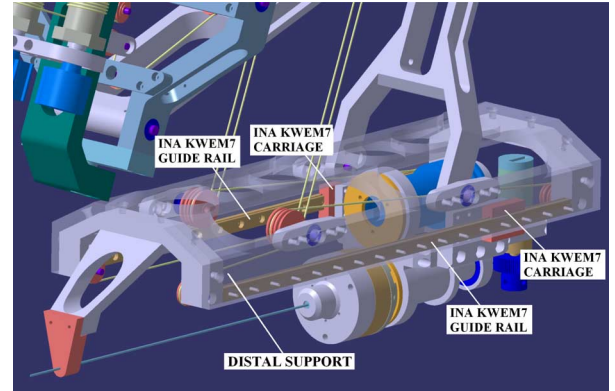


Fig. 7. Prismatic joint for needle translation.

termination points (OutputDrum), provides needle attachment point (RotaryLink), holds a (fifth) smaller motor for the stylet drive (DistalFrame), and provides a windup mechanism for the force sensor electrical cable (OutputDrum and RotaryLink).

The fifth motor (Maxon RE-max 17 with GP16A 19:1 gearbox and 512 CPR encoder) provides the stylet motion through the use of a rack and pinion transmission (SH1MS2B6F7A pinion with 63 teeth and RRS061M500 rack with 1-mm pitch from Reliance Precision Mechatronics, U.K.). The maximum travel length for the stylet motion was limited to 40 mm, based on the fact that each needle carries a maximum of five seeds with five spacers, each 4 mm in length. The rack and pinion gearing in combination with a linear bearing creates a prismatic joint for the stylet. The needle assembly holds an off-the-shelf 6-DOF hollow force sensor (ATI industrial automation, Nano-43, SI-18-0.25). The preloaded needle is mounted on the manipulator such that the stylet passes through the center bore of the force sensor and is rigidly attached to the tool flange of the force sensor. Once the needle tip is at the target, the needle assembly is retracted while simultaneously actuating the pinion in opposite direction to push the stylet and drop the seeds. It has been shown [15] that the rotation of the needle while it is being inserted can reduce needle tip deflection. To exploit this, the manipulator is designed to provide the rotation of the needle. Fig. 8 shows the CAD model of rack and pinion drive for needle stylet motion.

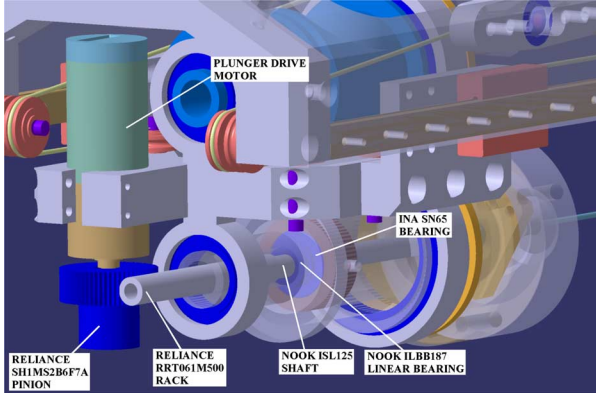


Fig. 8. Rack and pinion drive for needle stylet.

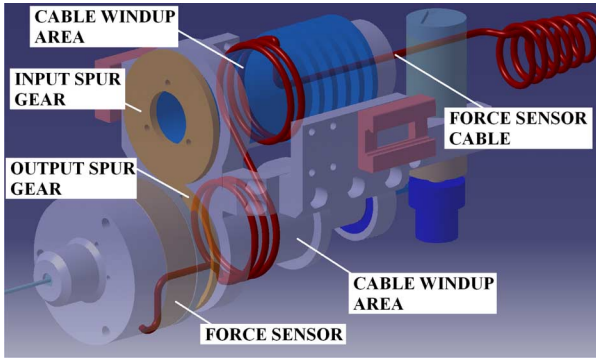


Fig. 9. Spur-gear based force sensor cable windup mechanism.

One problem that arises from rotating the needle about its axis is that the force sensor has to be rotated along with the needle. If left unattended, this could cause the force sensor electrical cable to wrap around the needle and interfere with its motion. In order to avoid this problem, OutputDrum and RotaryLink have an electrical cable windup mechanism such that force sensor cable transfers from one windup area to another as the needle is rotated about its axis. This is accomplished by incorporating 1:1 spur gears that rotate OutputDrum and RotaryLink in opposite directions. Fig. 9 shows the CAD model of the force sensor cable windup mechanism.

Fig. 10 shows the assembled micro-manipulator. The preliminary mechanical design of the manipulator has been reported in [45].

D. Gravity Balancing

One of the critical requirements for the micro-manipulator was to gravity balance the first two joints (largest joints) for enhanced safety. Conventionally, in a double-parallelogram-based mechanism counterbalancing about the first axis is achieved through the use of counterweights and about the second axis by either employing counterweights, as in [40], or utilizing the second RCM actuator as a partial counterbalance with the addition of springs and weights, as in [42]. For the micro-manipulator, active gravity balancing was implemented for the first axis. Partial spring balancing was selected for the second RCM axis and the remaining balancing torque was supplied by the second actuator.



Fig. 10. Fully assembled micro-manipulator.

ator. This approach resulted in the lightest possible manipulator, while achieving static balancing throughout the manipulator's workspace.

Dynamic simulations were conducted with SimDesigner to compute the gravity compensation torque at various configurations throughout the manipulator's workspace for the first two joints. A spring with a free length of 60 mm was selected for the simulations and the implementation. The spring constant of the actual spring was experimentally measured by loading the spring with known weights and recording the displacement. MATLAB was then utilized to perform curve fitting to the data, and the spring constant was measured as 0.72 N/mm and this value was used in the simulations. In this case, the gravity balancing torque is shared between the spring and the joint 2 actuator.

For joint 1 (first RCM axis), the gravity torque varies quite linearly with joint angle and a linear fit approximated for the gravity term with good accuracy for this joint. For joint 2 (second RCM axis), a 2-D curve fitting utilizing MATLAB was performed to approximate the gravity term. MATLAB was also utilized to obtain symbolic equations for gravity terms for the first and second joints.

Equations (6) and (7) show the symbolic expression for gravity terms (in newtons millimeter) on joints 1 and 2, respectively

$$G1 = 19.827 \theta_1 + 25.87 + G2 \quad (6)$$

$$G2 = C_1 \theta_2 + C_2 \quad (7)$$

with

$$\begin{aligned} C_1 &= -43.496 \\ C_2 &= -4.6828 d_3 + 1188.7 \end{aligned}$$

where θ_1 and θ_2 are joint 1 and 2 angles, respectively, and d_3 is the linear position of the needle translation assembly. These gravity terms were then experimentally verified on the manipulator and were found to give good results.

E. Joint Coupling

In the micro-manipulator, the RCM actuators (for joints 1 and 2) are located on the stationary part of the manipulator. As a result, there is coupling between these two axes. In other words, joint 2 can be independently actuated without affecting joint 1 encoder readings. However, any motion of joint 1 results in encoder counts from joint 2 as well. To compensate for these unwanted counts, joint 2 has to be simultaneously actuated (along with joint 1) in the opposite direction by a certain amount. To measure this coupling parameter, experiments were conducted with joint 2 physically locked in place to eliminate any contributions from the motion of joint 2. Thus, any encoder 2 readings were only a result of J1–J2 coupling. Joint 1 was moved from one extreme to the other and the encoder counts on both joints were recorded. MATLAB was utilized to perform curve fitting on encoder 2 data to compute a symbolic expression for joint coupling.

The closed-form equation for the J1–J2 coupling is

$$E2CP = 82.249 \theta_1 + 0.29787. \quad (8)$$

The corrected value of encoder 2 reading is thus given as

$$E2 = E2RAW + E2CP \quad (9)$$

where $E2RAW$ is the raw encoder reading and $E2CP$ is the effect from J1–J2 coupling.

For joints 3 and 4, a coupling matrix relates the actuator space to joint space. The elements relating θ_{m3} and θ_{m4} to the linear position of the needle translation assembly (d_3) were measured experimentally by actuating the joints 3 and 4 (equal amount in same direction) and measuring the resulting position of the needle assembly using a precision coordinate measuring device. The elements relating θ_{m3} and θ_{m4} to needle orientation (θ_4) were measured by actuating θ_{m3} and θ_{m4} until a complete revolution was observed at θ_4 (using a sharp knife edge etched on both DistalFrame and OutputDrum, see Fig. 6)

$$\begin{bmatrix} d_3 \\ \theta_4 \end{bmatrix} = \begin{bmatrix} -0.19757 \\ 0 \end{bmatrix} - \begin{bmatrix} \frac{1}{2GR_3} & \frac{1}{2GR_3} \\ \frac{1}{2GR_4} & \frac{1}{2GR_4} \end{bmatrix} \begin{bmatrix} \theta_{m3} \\ \theta_{m4} \end{bmatrix} \quad (10)$$

where θ_{m3} and θ_{m4} are actuator 3 and 4 angles (expressed in degrees), respectively. d_3 is the linear position of the needle translation assembly (expressed in meters) and θ_4 is the needle orientation (expressed in degrees). GR_3 and GR_4 are the gear ratios for the third and fourth joints of the manipulator as outlined in the next section.

TABLE I
EXPERIMENTAL DATA TO COMPUTE GEAR RATIO

Joint No.	Max. Joint Motion (MJM)	Total No. of Pulses (TNP)
1	$\pm 23.36^\circ$	3901
2	$\pm 13.83^\circ$	2305
3	160 mm	5500
4	$\pm 180^\circ$	2358

TABLE II
GEAR RATIOS AND THEORETICAL RESOLUTION

Joint	Gear Ratio	Resolution (Calculated)
1	15.024	0.011°
2	14.993	0.012°
3	$6.187 \frac{\text{deg}}{\text{mm}}$	0.029mm
4	1.178	0.152°
5	$5.714 \frac{\text{deg}}{\text{mm}}$	0.0016mm

F. Gear Ratios

As opposed to a conventional gear train, it is difficult to compute an exact gear ratio for a cable-based transmission from a CAD model due to factors such as flexibility in the stainless steel cable, manufacturing tolerances, etc. Thus, the exact gear ratio is experimentally determined for such mechanisms. For joints 1 and 2, the manipulator was moved from one joint limit to another, and the number of encoder pulses was recorded. The numerical value for the maximum joint motion (MJM) for these joints was computed from the CAD model. For joint 3, MJM represents the measured value using the coordinate measuring device and TNPs are the corresponding encoder counts (either M3 or M4). For joint 4, TNP represents the encoder pulses for a complete revolution. The first four joints of the micro-manipulator are equipped with 500 CPR encoders that provide 2000 pulses after quadrature decoding.

For the first four joints, the gear ratio can be computed as (Table I)

$$GR_{\{1-4\}} = \frac{\text{TNP} \times 360}{2000 \times \text{MJM}}. \quad (11)$$

For joint 5, the linear motion of the stylet is accomplished through a rack and pinion transmission. The gear ratio (in degrees per millimeter) in this case is given by

$$GR_5 = \frac{360}{\text{NPT} \times P} \quad (12)$$

where NPT = number of pinion teeth and P = pitch of the rack and pinion. In this case, NPT = 63 and P = 1 mm. Table II shows the computed gear ratios and the theoretical positioning resolution for each joint of the micro-manipulator.

V. MANIPULATOR KINEMATICS AND CONTROL

A. Forward Kinematics

The kinematic equations of the manipulator were derived using the conventions given in [46] and frame assignment shown in Fig. 2. Based on the frame assignment of Fig. 2, the Denavit–Hartenberg (D–H) parameters for the manipulator are given in Table III.

TABLE III
D-H PARAMETERS FOR MICRO-MANIPULATOR

i	α_{i-1}	a_{i-1}	d_i	θ_i
1	0	0	0	θ_1
2	-90°	0	0	$\theta_2 + 111.224^\circ$
3	90°	0	$-0.19757 + d_3$	0
4	0	0	0	θ_4

Note that the addition of 111.224° to the value of θ_2 in Table III represents the initial configuration of the manipulator (as shown in Fig. 2). Similarly, the addition of -0.19757 to the value of d_3 represents the initial offset of the needle translation assembly. The fifth joint axis (for stylus motion) aligns with the needle longitudinal axis and does not affect the kinematics of the manipulator, and thus is not included in Table III. That joint can be independently actuated as the needle sheath is extracted to deliver seeds.

From Table III, the transformation that relates frame {4} to frame {0} is given as [46]

$${}^0T_4 = \begin{bmatrix} c_1 c_2 c_4 - s_1 s_4 & -c_1 c_2 s_4 + s_1 c_4 & c_1 s_2 & c_1 s_2 d_3 \\ s_1 c_2 c_4 + c_1 s_4 & -s_1 c_2 s_4 + c_1 c_4 & s_1 s_2 & s_1 s_2 d_3 \\ -s_2 c_4 & s_2 s_4 & c_2 & c_2 d_3 \\ 0 & 0 & 0 & 1 \end{bmatrix} \quad (13)$$

where d_3 = linear travel of the needle, $c_1 = \cos(\theta_1)$, and $s_1 = \sin(\theta_1)$. The final transformation relating frame {T} to frame {B} can be computed as

$${}^B T_T = {}^B T_0 {}^0 T_4 {}^4 T_T. \quad (14)$$

B. Inverse Kinematics

For a given 0T_4 , the inverse kinematics for the micro-manipulator are given as

$$\begin{aligned} \theta_1 &= \text{atan} 2(T_{24}, T_{14}) \\ \theta_2 &= \text{atan} 2(\sqrt{T_{14}^2 + T_{24}^2}, T_{34}) \\ d_3 &= -|\sqrt{T_{14}^2 + T_{24}^2 + T_{34}^2}| \\ \theta_4 &= \text{atan} 2(T_{32}, -T_{31}). \end{aligned} \quad (15)$$

It was found that inside the manipulator workspace, (15) provides a unique solution, and thus, can be directly solved to compute a set of joint angles for a given end-effector pose.

C. Manipulator Jacobian

The equation relating joint velocities to end-effector velocities is given as

$$\dot{x} = {}^0J \dot{\theta} \quad (16)$$

with

$$\begin{aligned} \dot{\theta} &= [\dot{\theta}_1 \quad \dot{\theta}_2 \quad \dot{d}_3 \quad \dot{\theta}_4]' \\ \dot{x} &= [\dot{X} \quad \dot{Y} \quad \dot{Z} \quad \dot{\phi}]' \end{aligned} \quad (17)$$

where \dot{X} , \dot{Y} , and \dot{Z} are the linear velocities along the X -, Y -, and Z -axis (at needle base), respectively, and $\dot{\phi}$ is the angular

velocity about X -axis. For the micro-manipulator, the manipulator Jacobian 0J is given by

$${}^0J = \begin{bmatrix} -s_1 s_2 d_3 & c_1 c_2 d_3 & c_1 s_2 & 0 \\ c_1 s_2 d_3 & s_1 c_2 d_3 & s_1 s_2 & 0 \\ 0 & -s_2 d_3 & c_2 & 0 \\ 0 & -s_1 & 0 & c_1 s_2 \end{bmatrix}. \quad (18)$$

D. Singularity Analysis

For the micro-manipulator, the determinant of (18) is given by

$$\text{DET}[{}^0J] = -\cos(\theta_1) \sin^2(\theta_2) d_3^2. \quad (19)$$

Thus, the micro-manipulator would be in a singular configuration at the following poses:

$$\begin{aligned} \theta_1 &= -\frac{\pi}{2}, \frac{\pi}{2} \\ \theta_2 &= 0, \pi \\ d_3 &= 0. \end{aligned} \quad (20)$$

Note that these values of θ_1 , θ_2 , and d_3 are outside the reachable workspace of the manipulator. Therefore, no singularity exists inside manipulator workspace.

E. Joint Space PID With Gravity Compensation

The dynamics of a manipulator can be represented as

$$\tau = M(\theta) \ddot{\theta} + V(\theta, \dot{\theta}) + G(\theta) \quad (21)$$

where $M(\theta)$ is the manipulator mass matrix, $V(\theta, \dot{\theta})$ contain the centrifugal and Coriolis terms, and $G(\theta)$ is the gravity term.

The task of percutaneous needle insertion is generally done using very slow motions with minimal acceleration. Thus, the effect of the velocity and acceleration terms on manipulator dynamics is also minimal. Therefore, for the micro-manipulator, the following control law is sufficient:

$$\tau = K_p e + K_d \dot{e} + K_i \int e dt + G(\theta) \quad (22)$$

with

$$\begin{aligned} e &= \theta_d - \theta \\ \dot{e} &= \dot{\theta}_d - \dot{\theta} \end{aligned} \quad (23)$$

where e and \dot{e} are the joint and velocity tracking errors, respectively. K_p , K_d , and K_i are the proportional, derivative, and integral gains, respectively.

F. High-Gain Observer

Because of the low velocities involved, ordinary differentiation to compute joint velocities from encoder readings leads to large amounts of noise in the computed velocity. In order to avoid this problem, a high-gain observer was implemented to approximate the joint velocities in the micro-manipulator.

TABLE IV
NUMERICAL VALUES FOR THE OBSERVER PARAMETERS

Joint	ϵ	α_1	α_2
1	0.0005	50	625
2	0.0005	50	625
3	1	30	225
4	1	30	225
5	1	30	225

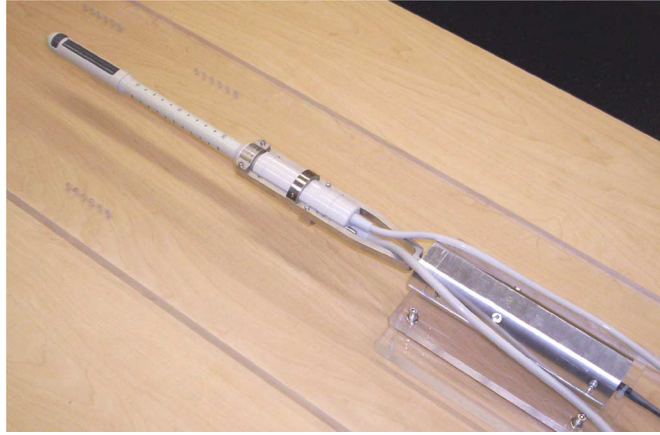


Fig. 11. Ultrasound rotator assembly.

Let us denote the joint angle as θ and the respective joint velocity as ω , the estimated value of the joint angle as $\hat{\theta}$, and the estimated joint velocity as $\hat{\omega}$. Then, the discretized observer equations are given by [47]

$$\begin{aligned}\hat{\theta}[kT] &= \frac{\epsilon\hat{\theta}[(k-1)T] + \epsilon T\hat{\omega}[(k-1)T] + \alpha_1 T\theta[kT]}{\epsilon + \alpha_1 T} \\ \hat{\omega}[kT] &= \hat{\omega}[(k-1)T] + \frac{\alpha_2 T}{\epsilon}(\theta[kT] - \hat{\theta}[kT])\end{aligned}\quad (24)$$

where ϵ is a positive number, k is the sampling instant, and T is the sampling period (1/1024). Positive constants α_1 and α_2 are selected such that the roots of the equation

$$s^2 + \alpha_1 s + \alpha_2 = 0 \quad (25)$$

have negative real parts. Table IV shows the numerical values for the observer parameters.

VI. 3-D ULTRASOUND

The experimental setup includes an Aloka SSD-1000 ultrasound system with a UST-672-5/7.5 biplane transrectal transducer. The video output from the ultrasound system is captured using a Matrox Meteor-II frame grabber card into a PC for further processing. The same PC also controls a custom-designed rotator assembly that rotates the ultrasound probe about its central axis. The assembly includes a zero-backlash motor (Faulhaber 2232U024 motor with a 879:1 gearhead and a 512 CPR encoder) for actuation and a rotary potentiometer to provide absolute angle measurements. A standard PID control law with static friction compensation was implemented for the rotator assembly. Fig. 11 shows the ultrasound rotator assembly.

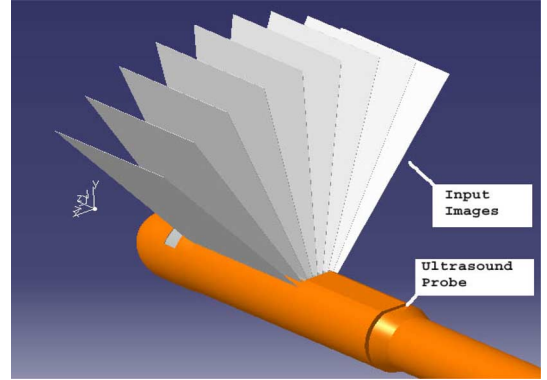


Fig. 12. Graphical representation of input images.

In order to create 3-D ultrasound images, a set of 100 2-D B-mode ultrasound images is acquired at 0.7° intervals as the probe is rotated about its axis by the rotator. These images appear as a fan (as shown in Fig. 12) with its central axis aligned with that of the ultrasound probe. Fig. 12 also shows the image coordinate system (z along the probe axis, y toward the top, and x to the left). Before these images can be read into any visualization software, they are required to undergo a polar to rectangular transformation. The reconstruction algorithm computes new pixel values on a 3-D Cartesian grid based on the pixel values from the input images acquired in the polar coordinate system. A destination-oriented method [48] is employed, where for each output pixel, the corresponding polar coordinates are computed. The pixel intensity from the nearest pixel in the polar coordinate image is then assigned to the output pixel.

For each z , let x, y be the coordinates of a point on the output Cartesian grid and r, θ the polar coordinates corresponding to that point. Then, for nearest neighbor interpolation, first a nearest input image is found corresponding to θ , and then, the nearest pixel in that image is found corresponding to r . The pixel intensity of that pixel is assigned to the output pixel at x, y, z .

At present, it takes a few minutes for the reconstruction algorithm to compute a new set of Cartesian images ($511 \times 446 \times 270$, with a voxel size of $0.2 \times 0.2 \times 0.2$ mm). Hence, no real-time tracking of the needle is performed.

VII. EXPERIMENTAL RESULTS

A. Joint Tracking Experiments

Joint space tracking experiments were conducted after the manipulator was completely assembled. In these experiments, each joint of the manipulator was commanded to follow a desired trajectory in free space. The desired trajectory was implemented as a linear segment with parabolic blends [49] with slow velocity profiles (as applicable in case of needle insertion). These experiments were performed with a single joint moving at a time while keeping others at fixed values, as would be the case in an actual robot-assisted brachytherapy procedure. The difference between commanded value and the actual joint value denotes the tracking error.

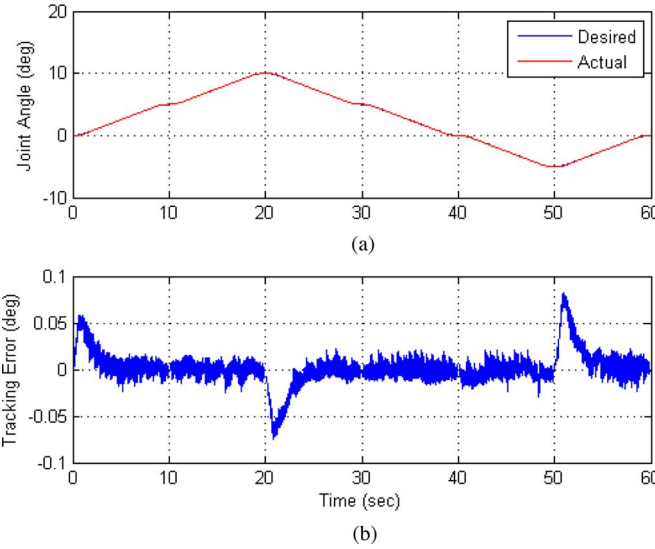


Fig. 13. Joint 1 tracking response using a PID controller for a multi-segment trajectory. (a) Joint tracking. (b) Tracking error.

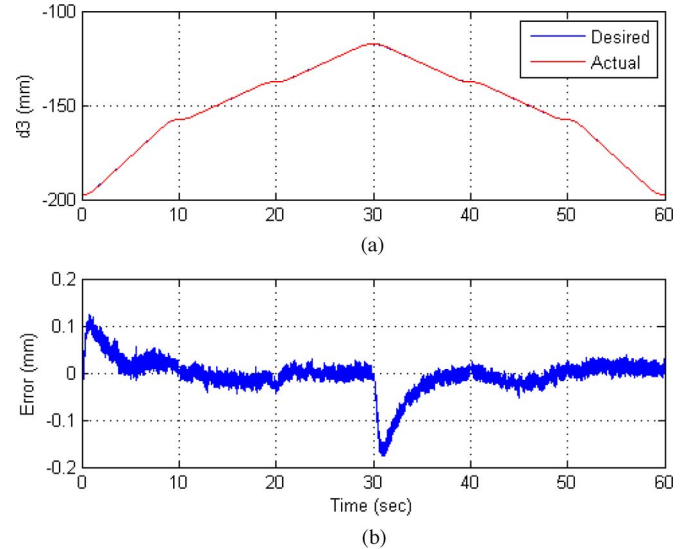


Fig. 15. Joint 3 tracking response using a PID controller for a multi-segment trajectory. (a) Joint tracking. (b) Tracking error.

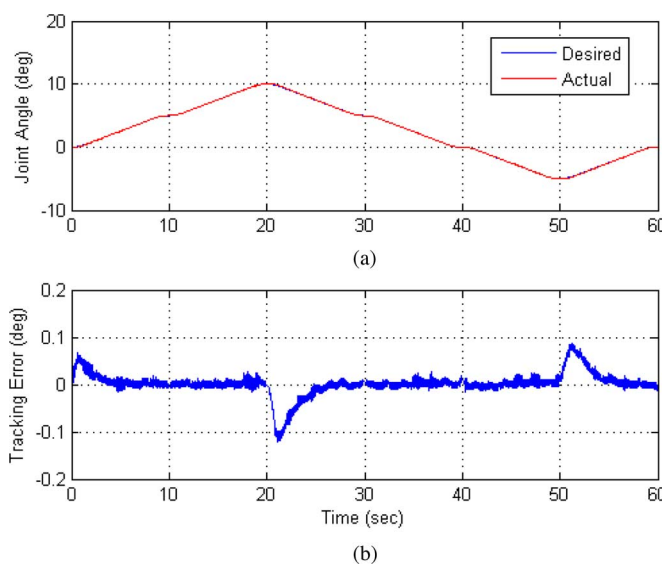


Fig. 14. Joint 2 tracking response using a PID controller for a multi-segment trajectory. (a) Joint tracking. (b) Tracking error.

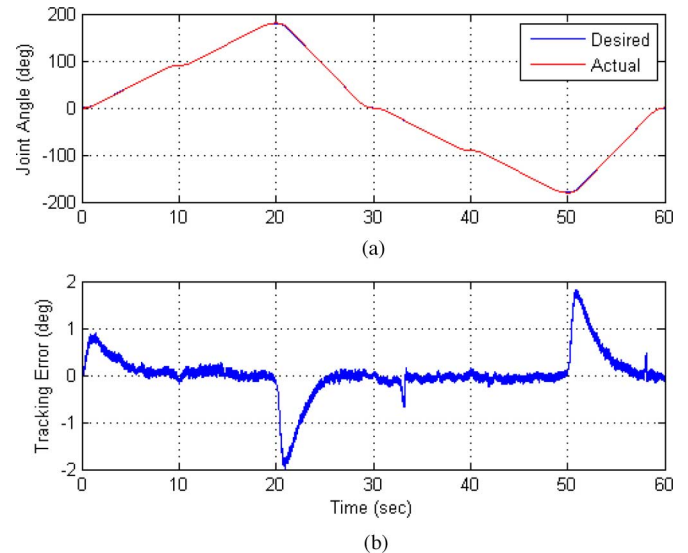


Fig. 16. Joint 4 tracking response using a PID controller for a multi-segment trajectory. (a) Joint tracking. (b) Tracking error.

Fig. 13 shows the joint tracking and the tracking error for the first joint of the micro-manipulator for a multiple segment trajectory. Similarly, Figs. 14–16 show the joint tracking and tracking errors for the second, third (needle translation), and fourth (needle rotation) joints of the manipulator, respectively. Various other trajectories (ranging from slow velocities to fast velocities) were tested on the manipulator, and it was found that the speed of the trajectory did not have much effect on the magnitude of the tracking error. It can be seen that a PID control law with gravity balance was able to follow the desired trajectory with good accuracy for all joints of the manipulator.

B. Free Air Positioning Experiments

In order to test the positioning accuracy of the manipulator in free space, the manipulator was mounted on a rigid stand. An XYZ coordinate measuring device with a resolution of 1 μm (Model 4765 from Parker Automation, USA) was also mounted on the same table. The coordinate measuring device was positioned in relation to the manipulator such that each point in the manipulator workspace could be measured using the device. A sharp pointer was mounted as an end-effector to the coordinate measuring device and was aligned with the needle tip at each target point to measure the actual coordinates of needle tip. Fig. 17 shows the experimental setup for measuring the positioning accuracy.

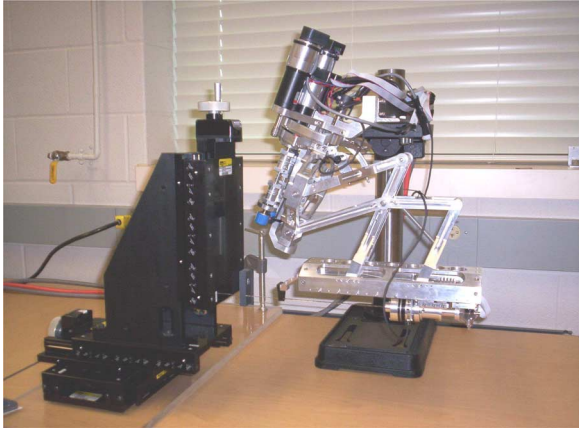


Fig. 17. Setup to measure positioning accuracy.

TABLE V
POSITIONING ERROR IN FREE AIR

Theta 1 (deg)	Theta 2 (deg)	RMS error (mm)
0	-13	0.39
0	13	0.48
19	-13	1.06
19	0	1.03
19	13	0.90
-19	-13	0.79
-19	0	0.69
-19	13	0.94

A PID control law (details given in Section V-E) was implemented on the manipulator and various points were targeted throughout its workspace (a sector-shaped volume). The needle positioning error was computed as

$$e_t = \sqrt{e_x^2 + e_y^2 + e_z^2} \quad (26)$$

where e_x , e_y , and e_z are the positioning errors measured along the X -, Y -, and Z -axis, respectively, and e_t is the calculated error. It was found that the positioning error was of the order of 1 mm at the workspace boundaries and smaller (< 1 mm) inside the workspace. Table V lists the free air errors at workspace boundaries (at a needle insertion depth of 120 mm).

C. Needle Insertion Experiments in Agar Phantoms

Figs. 18 and 19 show the system block diagram and experimental setup, respectively. The system consists of an imaging computer to capture and visualize ultrasound images and another computer to control the micro-manipulator. The two computers are interfaced to each other through a Transmission Control Protocol (TCP)/IP connection over ethernet. However, at present, the information flow is only from the imaging computer to the control computer.

The micro-manipulator was mounted on manually driven XYZ stages for the experiments reported in this paper. These stages have 1- μm resolution and allow for functional testing of the micro-manipulator. Later, the macro-manipulator [50] will be utilized to carry the micro-manipulator and position it at the skin entry point. Fig. 20 shows the micro- and macro-manipulators mounted together.

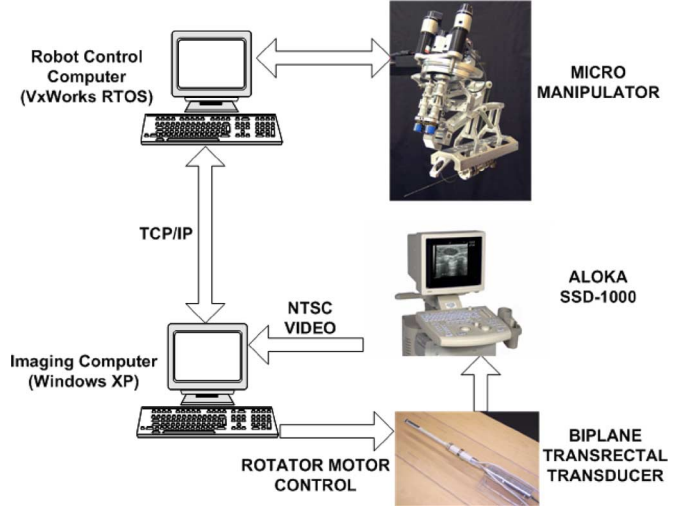


Fig. 18. System block diagram.

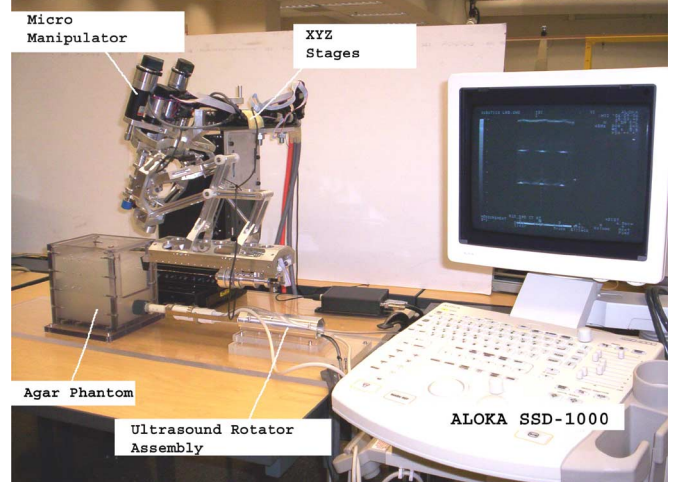


Fig. 19. Experimental setup.

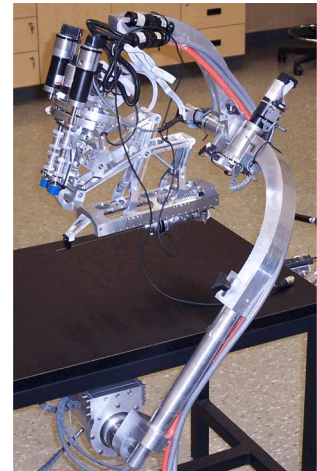


Fig. 20. Micro manipulator mounted on the macro-manipulator.

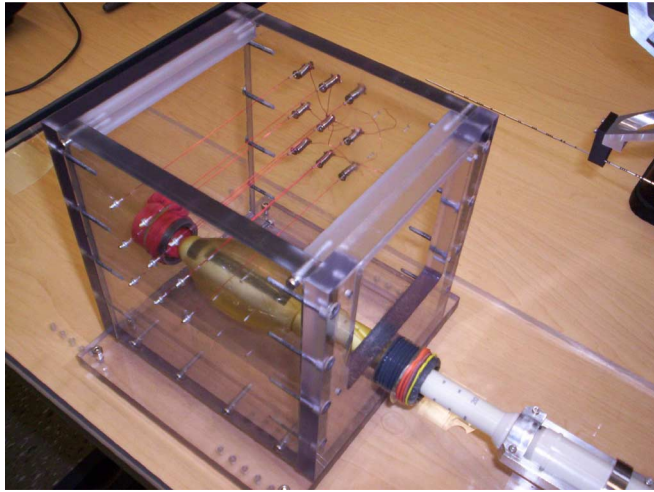


Fig. 21. Custom-built container for ultrasound calibration and needle insertion experiments.

A custom-built container was utilized to make agar phantoms for the experiments. One wall of the container has a removable (100 × 100 mm) window through which the needle is inserted. The container also includes a hole to denote the rectum and accommodate the ultrasound probe. The same container was also utilized to calibrate the ultrasound system. Two opposite sides of this container were machined with rectangular grids of holes (3 × 5 grid with each hole of 0.5 mm diameter) separated by 30 mm in the first direction and 20 mm in the second direction. In order to calibrate the ultrasound system, 0.35-mm-diameter copper wires were stretched across these holes, and then scanned in a water bath. Pixels per millimeter values for the ultrasound system were then computed by comparing the measured distances (in image coordinates) to the actual distances. Fig. 21 shows a close-up view of the container.

The ultrasound probe was registered to the container by mounting both the probe and the container to the same precision machined base. To register the manipulator to the container, the window in the container was removed and the XYZ stages were utilized to manually touch needle tip to various wires and edges of the container. Once this was accomplished, any target point given in the image coordinates could be easily translated to the robot's coordinate system.

The steps involved in targeting a point are as follows.

- 1) A prescan is performed as the ultrasound probe is rotated $\pm 35^\circ$ and images are acquired and saved onto hard disk.
- 2) The reconstruction algorithm loads these images into memory and computes a new set of Cartesian images based on the nearest neighbor interpolation.
- 3) The user loads the reconstructed images into the 3-D SLICER [51] software for visualization and defines a target point.
- 4) The coordinates of the target point are sent to the control computer through a TCP/IP connection.
- 5) The control software performs bound checking on the target point and executes the desired trajectory to bring the needle tip to the target point. The trajectory is executed in two steps: a) the RCM stage orients the needle along

TABLE VI
TARGET POINTS AND RESPECTIVE ERROR

Label	Insertion Depth (mm)	RMS error (mm)
P1	47.70	1.23
P2	51.19	0.56
P3	67.70	1.13
P4	68.58	0.97
P5	70.21	1.92
P6	71.77	2.04
P7	71.84	1.56
P8	71.84	1.28
P9	87.70	1.40
P10	89.00	0.56
P11	90.62	2.97
P12	90.93	1.34
P13	90.93	1.60
P14	90.93	1.75

the desired insertion path and b) the distal stage translates and/or rotates the needle toward the target.

- 6) Another full scan and interpolation is performed and the data are saved to verify the targeting accuracy later.
- 7) Steps 3–6 are repeated for each of the remaining target points.

An 18-G 20-cm bevel-tip brachytherapy needle (Cook Urological, Spencer, IN) was mounted on the manipulator for the experiments. The phantom was created with a mixture (% weight): water (98.25%), and Gelrite gellan gum (1.75%) (Sigma-Aldrich, St. Louis, MO).

A total of 14 target points was selected at various insertion depths and angulation values for the experiment. The points were selected so as to cover the clinically relevant workspace to validate the applicability of the manipulator. Upward tilting trajectories were also performed to demonstrate the avoidance of pubic arch interference. For the first RCM axis, the angulation values varied from -22.7° to $+17.89^\circ$. For the second RCM axis, the angulation values covered a range from -10.37° to $+12.65^\circ$. The needle insertion depth varied from 47.7 to 90.93 mm.

In order to verify the needle insertion accuracy, a postscan was carried out after the needle reached the targeted depth. The reconstructed data were then loaded into 3-D SLICER, and the needle tip was manually segmented in three orthogonal slices (referred to as the axial, sagittal, and coronal planes in 3-D SLICER). The axial, sagittal, and coronal planes were manually translated until satisfactory visualization of the needle tip was achieved. These three pixel coordinates were then assigned as the needle tip.

The pixel rms error between the needle tip coordinates and the targeted point was computed and given by

$$e_p = \sqrt{S^2 + R^2 + A^2} \quad (27)$$

where S , R , and A are the pixel errors in the axial, sagittal, and coronal planes, respectively. The rms error was then converted into millimeters by multiplying by 0.2 (voxel size).

The average rms targeting error was found to be 1.45 mm and the average insertion depth was 75.78 mm. A total of 85.7% of the needle insertions were within less than 2 mm error. Table VI shows the targeted point and respective targeting error.

VIII. DISCUSSION

Various sources of system errors were also briefly analyzed. For the joint tracking experiments, it was found that the encoder resolution imposes a limit on the resolution of the joint angle measurements. The off-the-shelf motors (with integrated brakes) employed on the first four joints of the manipulator were only available with a limited encoder resolution (500 CPR). This limitation can be eliminated through the integration of custom encoders with higher resolution on these motors.

For joint 4 (needle rotation), the relatively high tracking error is a result of high friction in the spur gear head employed at this joint and the drag resulting from the force sensor electrical cable. However, the magnitude of the error is within acceptable limits and has negligible effect on the seed placement accuracy. This error can be minimized to a certain extent by employing a timing belt transmission as opposed to spur gears and proper adjustment of belt tension to minimize friction.

During the needle positioning experiments, a small amount of needle deflection was also observed (due to gravity effects on the needle) and the reported results include those errors as well. This effect was found to be dominant at workspace extremities due to the large unsupported needle length in free air. It is anticipated that for needle insertion into the actual tissue, the needle deflection will be influenced to a large extent by needle-tissue interaction.

One limitation of this prototype is the large diameter of the off-the-shelf force sensor. This diameter was the deciding factor in selecting the distance between the lowest target point and the ultrasound probe due to the possibility of the robot colliding with the transducer. A custom-designed force sensor with a smaller diameter could solve this problem and is being investigated.

IX. CONCLUSION

In this paper, the design of a novel manipulator for prostate brachytherapy was described. The design of the manipulator was conducted following extensive discussions with clinicians and the formal requirements for the manipulator were based on their feedback. The manipulator has a total of 5 DOF: two for orientation, one each for translation and rotation of the needle and stylet motion to place the radioactive seeds. Some of the key characteristics of the manipulator are backdrivable joints, stationary actuators, fault tolerant needle driver, low-friction transmission, and a counterbalanced mechanism.

Numerous experiments were conducted to measure manipulator characteristics such as gear ratios, coupling parameters, and positioning accuracy. Once this was accomplished, the needle tip could be guided to the target consistently and accurately. The joint tracking experiments provided an insight into the performance of the control algorithm and its ability to track a given trajectory in free space. The needle targeting experiments proved that the manipulator was capable of positioning the needle tip at the target location with good accuracy (within 2 mm error).

Although the micro-manipulator was specifically developed for prostate brachytherapy, with minor modifications, the system can be adapted for delivering other forms of therapies such as

radio-frequency ablation and cyrotherapy. The manipulator was designed in a collaborative project with another research group that has developed custom dosimetry software for brachytherapy [51]. Work is in progress to integrate the manipulator and the dosimetry software in a single framework. It is hypothesized that the resulting system could allow dosemetry planning and therapy to be performed in a single session, and therefore could cut down on the procedure time and may lead to a dynamic intraoperative prostate brachytherapy procedure that is consistent and less operator-dependent.

REFERENCES

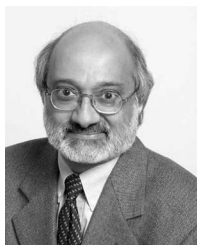
- [1] "Cancer Facts & Figures 2008," Amer. Cancer Soc., Atlanta, GA, Tech. Rep., 2008.
- [2] L. Garfinkel and M. Mushinski, "Cancer incidence, mortality and survival: Trends in four leading sites," *Stat. Bull. Metrop. Insur. Co.*, vol. 75, no. 3, pp. 19–27, 1994.
- [3] H. H. Holm, N. Juul, J. F. Pederson, H. Hansen, and I. Stroyer, "Transperineal 125iodine seed implantation in prostatic cancer guided transrectal ultrasonography," *Urology*, vol. 130, no. 1, pp. 283–286, 1983.
- [4] D. Ash, D. M. Bottomley, and B. M. Carey, "Prostate brachytherapy," *Prostate Cancer Prostate Dis.*, vol. 1, pp. 185–188, 1998.
- [5] (2003). [Online]. Available: www.patienthealthinternational.com
- [6] K. R. Bradizamani, K. Wallner, S. Sutlief, W. Ellis, J. Blasko, and K. Russell, "Anticipating poststatic volume changes due to prostate brachytherapy," *Radiat. Oncol. Investig.*, vol. 7, no. 6, pp. 360–364, 1999.
- [7] S. D. Pathak, P. D. Grimm, V. Chalana, and Y. Kim, "Pubic arch detection in transrectal ultrasound guided prostate cancer therapy," *IEEE Trans. Med. Imag.*, vol. 17, no. 5, pp. 762–771, Oct. 1998.
- [8] E. M. Messing, J. B. Zhang, D. J. Rubens, R. A. Brasacchio, J. G. Strang, A. Soni, M. C. Schell, P. G. Okuniff, and Y. Yu, "Intraoperative optimized inverse planning for prostate brachytherapy: Early experience," *Int. J. Radiat. Oncol. Biol. Phys.*, vol. 44, no. 4, pp. 801–808, 1999.
- [9] Y. Yamada, L. Potters, M. Zaider, G. Cohen, E. Venkatraman, and J. Michael, "Impact of intraoperative edema during transperineal permanent prostate brachytherapy on computeroptimized and preimplant planning techniques," *Amer. J. Clin. Oncol.*, vol. 26, no. 5, pp. 130–135, 2003.
- [10] G. Fichtinger, E. C. Burdette, A. Tanacs, A. Patriciu, D. Mazilu, L. L. Whitcomb, and D. Stoianovici, "Robotically assisted prostate brachytherapy with transrectal ultrasound guided-phantom experiments," *Brachytherapy*, vol. 5, no. 1, pp. 91–98, 2006.
- [11] G. Fichtinger, T. L. DeWeese, A. Patriciu, A. Tanacs, D. Mazilu, J. A. Anderson, K. Masamune, R. H. Taylor, and D. Stoianovici, "System for robotically assisted prostate biopsy and therapy with intraoperative CT guidance," *J. Acad. Radiol.*, vol. 9, no. 1, pp. 60–74, 2002.
- [12] A. Patriciu, D. Stoianovici, and L. Whitcomb, "Motion-based robotic instrument targeting under C-arm fluoroscope," *Lect. Notes Comput. Sci.*, vol. 1935, pp. 988–998, 2000.
- [13] L. Phee, D. Xaio, J. Yuen, C. F. Chan, H. Ho, C. H. Thng, C. Cheng, and W. S. Ng, "Ultrasound guided robotic system for transperineal biopsy of the prostate," in *Proc. IEEE Int. Conf. Robot. Autom.*, 2005, pp. 1327–1332.
- [14] G. Megali, O. Tonet, C. Stefanini, M. Boccadoro, V. Papaspyropoulos, L. Angelini, and P. Dario, "A computer-assisted robotic ultrasound-guided biopsy system for video-assisted surgery," in *Proc. Int. Conf. Med. Image Comput. Comput.-Assisted Intervention (MICCAI)*, 2001, pp. 343–350.
- [15] B. L. Davies, S. J. Harris, and E. Dibble, "Brachytherapy—An example of a urological minimally invasive robotic procedure," *Int. J. Med. Robot. Comput. Assisted Surg.*, vol. 1, no. 1, pp. 88–96, 2004.
- [16] G. Kronreif, M. Fürst, J. Kettenbach, M. Figl, and R. Hanel, "Robotic guidance for percutaneous interventions," *J. Adv. Robot.*, vol. 17, no. 6, pp. 541–560, 2003.
- [17] G. Kronreif, J. Kettenbach, M. Fürst, M. Kornfeld, W. Ptacek, and M. Vogele, "IntraROB—A programmable targeting device for interventional radiology," in *Proc. 19th Int. Congr. Comput. Assisted Radiol. Surg. (CARS)*, 2005, vol. 1281, pp. 407–411.

- [18] J. Hong, T. Dohi, M. Hashizume, K. Konishi, and N. Hata, "An ultrasound-driven needle insertion robot for percutaneous cholecystostomy," *Phys. Med. Biol.*, vol. 49, no. 3, pp. 441–455, 2004.
- [19] T. K. Podder, J. Sherman, D. P. Clark, E. M. Messing, D. J. Rubens, J. G. Strang, L. Liao, R. A. Brasacchio, Y. Zhang, W. S. Ng, and Y. Yu, "Evaluation of robotic needle insertion in conjunction with in vivo manual needle insertion in the operating room," in *Proc. IEEE Workshop Robots Hum. Interactive Commun.*, 2005, pp. 66–72.
- [20] A. Krieger, R. C. Susil, C. Menard, J. A. Coleman, G. Fichtinger, E. Atalar, and L. L. Whitcomb, "Design of a novel MRI compatible manipulator for image guided prostate interventions," *IEEE Trans. Biomed. Eng.*, vol. 52, no. 2, pp. 306–313, Feb. 2005.
- [21] S. Okazawa, R. Ebrahimi, J. Chuang, S. E. Salcudean, and R. Rohling, "Hand-held steerable needle device," *IEEE Trans. Mechatronics*, vol. 10, no. 3, pp. 285–296, Jun. 2005.
- [22] Y. Yu, T. Podder, Y. Zhang, W. S. Ng, V. Misic, J. Sherman, L. Fu, D. Fuller, E. Messing, D. Rubens, J. Strang, and R. Brasacchio, "Robot-assisted prostate brachytherapy," in *Proc. Int. Conf. Med. Image Comput. Comput.-Assisted Intervention*, 2006, vol. 4190, pp. 41–49.
- [23] S. E. Salcudean, T. D. Prananta, W. J. Morris, and I. Spadinger, "A robotic needle guide for prostate brachytherapy," in *Proc. IEEE Int. Conf. Robot. Autom.*, 2008, pp. 2975–2981.
- [24] M. H. Loser and N. Navab, "A new robotic system for visually controlled percutaneous interventions under CT fluoroscopy," in *Proc. Int. Conf. Med. Image Comput. Computer-Assisted Interventions (MICCAI)*, 2000, pp. 887–896.
- [25] B. Maurin, C. Doignon, J. Gangloff, B. Bayle, M. Mathelin, O. Piccin, and A. Gangi. (2005). CTBot: A stereotactic-guided robotic assistant for percutaneous procedures of the abdomen. *Proc. SPIE Med. Imag.* [Online]. 5744(1), pp. 241–250. Available: <http://link.aip.org/link/?PSI/5744/241/1>
- [26] B. Maurin, B. Bayle, O. Piccin, J. Gangloff, M. de Mathelin, C. Doignon, P. Zanne, and A. Gangi, "A patient-mounted robotic platform for CT-scan guided procedures," *IEEE Trans. Biomed. Eng.*, vol. 55, no. 10, pp. 2417–2425, 2008.
- [27] K. Chinzei and K. Miller, "Towards MRI guided surgical manipulator," *Int. Med. J. Exp. Clin. Res.*, vol. 7, no. 1, pp. 153–163, 2001.
- [28] E. Christoforou, E. Akbudak, A. Ozcan, M. Karanikolas, and N. V. Tsekos, "Performance of interventions with manipulator-driven real-time MR guidance: Implementation and initial in vitro tests," *Med. Reson. Imag.*, vol. 25, no. 1, pp. 69–77, 2007.
- [29] N. V. Tsekos, J. Shudy, E. Yacoub, P. V. Tsekos, and I. G. Koutlas, "Development of a robotic device for MRI-guided interventions in the breast," in *Proc. IEEE 2nd Int. Symp. Bioinf. Bioeng.*, 2001, pp. 201–208.
- [30] H. Elhawary, A. Zivanovic, M. Rea, B. Davies, C. Besant, D. McRobbie, N. Souza, I. Young, and M. Lamperth, "The feasibility of MR-image guided prostate biopsy using piezoceramic motors inside or near to the magnet isocentre," in *Proc. Int. Conf. Med. Image Comput. Computer-Assisted Interventions (MICCAI)*, 2006, vol. 4190, pp. 519–526.
- [31] M. Muntener, A. Patriciu, D. Petrisor, D. Mazilu, H. Bagga, L. Kavoussi, K. Cleary, and D. Stoianovici, "Magnetic resonance imaging compatible robotic system for fully automated brachytherapy seed placement," *Adult Urol.*, vol. 68, pp. 1313–1317, 2006.
- [32] G. S. Fischer, I. Iordachita, C. Csoma, J. Tokuda, S. P. DiMaio, C. M. Tempany, N. Hata, and G. Fichtinger, "MRI-compatible pneumatic robot for transperineal prostate needle placement," *IEEE Trans. Mechatronics*, vol. 13, no. 3, pp. 295–305, Jun. 2008.
- [33] A. A. Goldenberg, J. Trachtenberg, W. Kucharczyk, Y. Yi, M. Haider, L. Ma, R. Weersink, and C. Raoufi, "Robotic system for closed-bore MRI-guided prostatic interventions," *IEEE Trans. Mechatronics*, vol. 13, no. 3, pp. 374–379, Jun. 2008.
- [34] N. C. Kheng, N. W. Sing, L. Phee, and C. Cheng, "A HIFU robot for transperineal treatment of prostate cancer," in *Proc. 7th Int. Conf. Control, Autom., Robot. Vis.*, 2002, pp. 560–565.
- [35] R. Locke, "Remote center-of-motion for robotics-assisted minimally-invasive surgery," Master's thesis, Univ. Western Ontario, London, ON, Canada, 2007.
- [36] Y. F. Wang, D. R. Uecker, and Y. Wang, "Choreographed scope manoeuvring in robotically-assisted laparoscopy with active vision guidance," in *Proc. IEEE Workshop Appl. Comput. Vis. (WACV)*, 1996, pp. 187–192.
- [37] M. J. H. Lum, J. Rosen, M. N. Sinanan, and B. Hannaford, "Optimization of spherical mechanism for a minimally invasive surgical robot: Theoretical and experimental approaches," *IEEE Trans. Biomed. Eng.*, vol. 53, no. 7, pp. 1440–1445, Jul. 2006.
- [38] J. Rosen, J. D. Brown, L. Chang, M. Barreca, M. Sinanan, and B. Hannaford, "The blue—A system for measuring the kinematics and the dynamics of minimally invasive surgical tools in-vivo," in *Proc. IEEE Int. Conf. Robot. Autom.*, 2002, pp. 1876–1881.
- [39] R. H. Taylor, J. Funda, B. Eldridge, S. Gomory, K. Gruben, D. LaRose, M. Talamini, L. Kavoussi, and J. Anderson, "A telerobotic assistant for laparoscopic surgery," *IEEE Eng. Med. Biol. Mag.*, vol. 14, no. 3, pp. 279–288, May/Jun. 1995.
- [40] P. Abolmaesumi, S. E. Salcudean, W. H. Zhu, M. R. Siroouspour, and S. P. DiMaio, "Image-guided control of a robot for medical ultrasound," *IEEE Trans. Robot. Autom.*, vol. 18, no. 1, pp. 11–23, Feb. 2002.
- [41] D. Stoianovici, K. Cleary, A. Patriciu, D. Mazilu, A. Stanimir, N. Craciunoiu, V. Watson, and L. Kavoussi, "Acubot: A robot for radiological interventions," *IEEE Trans. Robot. Autom.*, vol. 19, no. 5, pp. 927–930, Oct. 2003.
- [42] A. J. Madhani, G. Niemeyer, and J. K. Salisbury, "The black falcon: A teleoperated surgical instrument for minimally invasive surgery," in *Proc. IEEE Int. Conf. Intell. Robots Syst.*, 1998, pp. 936–944.
- [43] A. C. Waspe, H. J. Cakiroglu, J. C. Lacefield, and A. Fenster, "Design and validation of a robotic needle positioning system for small animal imaging applications," in *Proc. IEEE Conf. Eng. Med. Biol. Soc.*, 2006, pp. 412–415.
- [44] J. K. Salisbury, W. Townsend, D. M. DiPietro, and B. S. Eberman, "Compact cable transmission with cable differential," U.S. Patent 5 046 375, 1991.
- [45] H. Bassan, R. V. Patel, and M. Moallem, "A novel manipulator for prostate brachytherapy: Design and preliminary results," in *Proc. 4th IFAC Symp. Mechatronics Syst.*, 2006, pp. 30–35.
- [46] J. Craig, *Introduction to Robotics: Mechanics and Control*. Reading, MA: Addison-Wesley, 1989.
- [47] H. Khalil, "Adaptive output feedback control of nonlinear systems represented by input-output models," *IEEE Trans. Autom. Control*, vol. 41, no. 2, pp. 177–188, Feb. 1996.
- [48] S. Tong, D. B. Downey, H. N. Cardinal, and A. Fenster, "A three-dimensional ultrasound prostate imaging system," *Ultrasound Med. Biol.*, vol. 22, no. 6, pp. 735–746, 1996.
- [49] R. V. Patel and Z. Lin, "Trajectory planning," in *International Encyclopedia of Robotics Applications and Automation*. New York: Wiley, 1988.
- [50] B. F. Yousef, R. V. Patel, and M. Moallem, "A macro-robot manipulator for medical applications," in *Proc. IEEE Int. Conf. Syst., Man Cybern.*, 2006, pp. 530–535.
- [51] (2007). [Online]. Available: www.slicer.org
- [52] A. Fenster, L. Gardi, Z. Wei, G. Wan, C. Edirisinghe, and D. B. Downey, "Robot-aided and 3D TRUS-guided intraoperative prostate brachytherapy," in *Basic and Advanced Techniques in Prostate Brachytherapy*, A. Dicker, L. Gomella, and G. Merrick, Eds. Boca Raton, FL: CRC, 2005, pp. 271–284.



Harmanpreet S. Bassan received the B.Eng. degree in electronics engineering from Nagpur University, Nagpur, India, in 1998, and the Ph.D. degree in electrical and computer engineering from The University of Western Ontario, London, ON, Canada, in 2007.

He is currently a Postdoctoral Fellow in the Department of Electrical and Computer Engineering, The University of Western Ontario, where he is also with the Canadian Surgical Technologies and Advanced Robotics (CSTAR). His current research interests include the design of mechatronic systems for minimally invasive surgery, design of haptic interfaces, robotics, and embedded and real-time systems.



Rajni V. Patel (M'76–SM'80–F'92) received the Ph.D. degree in electrical engineering from the University of Cambridge, Cambridge, U.K., in 1973.

He is currently a Distinguished University Professor and a Tier-1 Canada Research Chair in the Department of Electrical and Computer Engineering, The University of Western Ontario, London, ON, Canada, with a cross appointment in the Department of Surgery, Schulich School Medicine and Dentistry. He is also the Director of Engineering for the Canadian Surgical Technologies and Advanced Robotics.

Prof. Patel is a Fellow of the American Society of Mechanical Engineers (ASME) and the Canadian Academy of Engineering. He was on the Editorial Boards of the IEEE TRANSACTIONS ON ROBOTICS, the IEEE/ASME TRANSACTIONS ON MECHATRONICS, and the IEEE TRANSACTIONS ON AUTOMATIC CONTROL. He is currently a member of the Advisory Board of the *International Journal of Medical Robotics and Computer Assisted Surgery*.



Mehrdad Moallem (M'95) received the B.Sc. degree in electrical engineering from Shiraz University, Shiraz, Iran, in 1986, the M.Sc. degree in electrical engineering from Sharif University of Technology, Tehran, Iran, in 1988, and the Ph.D. degree in electrical engineering from Concordia University, Montreal, QC, Canada, in 1997.

From 1997 to 2007, he was a Postdoctoral Researcher at Concordia University and Duke University, Durham, NC. From 1999 to 2007, he was a faculty member in the Department of Electrical and Computer Engineering, The University of Western Ontario, London, ON, Canada. He is currently an Associate Professor in the School of Engineering, Simon Fraser University, Surrey, BC, Canada. His current research interests include the general area of control applications including control of structurally flexible systems, smart sensors and actuators, advanced robotic and mechatronic systems, and embedded real-time computing.